CrossMark

TNO or Comet? The Search for Activity and Characterization of Distant Object 418993 (2009 MS9)

Erica Bufanda[1] , Karen J. Meech[1] , Jan T. Kleyna[1] , Olivier R. Hainaut[2] , James M. Bauer[3] , Haynes Stephens[4] , Peter Veres[5], Marco Micheli[6,7] , Jacqueline V. Keane[1] , Robert Weryk[1] , Richard Wainscoat[1] , Devendra K. Sahu[8] , and Bhuwan C. Bhatt[8]

[1] Institute for Astronomy, 2680 Woodlawn Drive, Honolulu, HI 96822 USA; ebufanda@hawaii.edu
[2] European Southern Observatory, Karl-Schwarzschild-Strasse 2, D-85748 Garching bei München, Germany
[3] Department of Astronomy, University of Maryland, College Park, MD 20742-2421, USA
[4] University of California, Berkeley, USA
[5] Harvard-Smithsonian Center for Astrophysics, 60 Garden Street, MS-15, Cambridge, MA 02138, USA
[6] ESA SSA-NEO Coordination Centre, Largo Galileo Galilei, 1, I-00044 Frascati (RM), Italy
[7] INAF–Osservatorio Astronomico di Roma, Via Frascati, 33, I-00040 Monte Porzio Catone (RM), Italy
[8] Indian Institute of Astrophysics, II Block, Koramangala, Bangalore 560 034, India

Abstract

The perihelion of the trans-Neptunian object (TNO) 2009 MS9 brings it close to the distance where some long-period comets are seen to become active. Knowing this, and the fact that this object appears to brighten in excess of its predicted nucleus brightness, suggests that 2009 MS9 has a delayed onset of activity brought on by the sublimation of a species more volatile than water. In this paper, we characterize 2009 MS9's physical properties and investigate potential outgassing through composite images, sublimation models, and measurements of spectral reflectivity. We find that deep composite images of the object at various epochs along its orbit show no evidence of dust yet place sensitive limits to the dust production. We estimate the nucleus radius to be 11.5 ± 3.5 km using thermal IR modeling from NEOWISE data and use this and data pre-perihelion to estimate a geometric albedo of 0.25. We compare a CO sublimation activity model to its post-perihelion heliocentric light curve and find that these data support an active fractional area of 5×10^{-6} assuming 2 μm–sized grains and other typical comet parameters. The spectral reflectivity of the surface materials obtained with the Gemini Observatory and CFHT at different epochs shows a reddening spectral slope. We compare the physical properties of 2009 MS9 to both TNO and comet populations and speculate that 2009 MS9's reddening may be due to the buildup of a dust mantle on the surface and could be an explanation of why TNOs exhibit a color bimodality.

1. Introduction

The distribution and migration of volatiles in the solar system from past to present is a topic of great interest in astronomy because of its intimate connection to early solar system dynamics and chemistry and thus the origin of water on Earth. The most optimal way to investigate the solar system volatile distribution is to study the physics of primitive minor bodies, i.e., asteroids and comets. Primitive undifferentiated bodies are the least transformed volatile "vehicles to the past"; because of their size, most lack the interior physical processes that obscure the chemical history imprinted since formation. Hence, comets and asteroids can be used as tracers to infer what occurred during the early solar system.

The volatiles that drive comet sublimation are H_2O, CO, and CO_2 ice (Meech & Svoren 2004). These molecules produce outgassing that drags dust particles from the nucleus surface and subsurface, often creating a visible coma that results in a change in brightness. This process becomes observable at different heliocentric distances characteristic of the volatile

latent heat of sublimation, the effective surface temperature of the nucleus, and the dust grain sizes (Meech & Svoren 2004).

For example, the maximum rate of water-ice sublimation occurs at 180 K but begins at lower rates with lower temperatures; hence, ice sublimation can begin to lift micron-sized dust that can be detected as far as 5–6 au from the Sun (Meech & Svoren 2004). For CO_2, this occurs near 20 au with a peak sublimation rate at 80 K, and for CO at 25 K, this occurs beyond 50 au, at a distance beyond the Kuiper Belt (Meech & Svoren 2004). These values assume that the volatiles are located at the surface. However, because of thermal processing from previous perihelion passages or cosmic-ray processing of comet surfaces prior to the comet entering the inner solar system for the first time, volatiles are likely buried beneath the surface and do not begin sublimating until the heat wave from the surface penetrates the lower layers (Prialnik et al. 2004).

Because of this, volatiles likely exist in the comet as either differentiated layers (as a result of phase transition, sublimation, and/or recondensation of ices) or pockets of crystalline or amorphous ice. In addition to traditional ice sublimation due to solar heating, outgassing brought on by an amorphous ice transition is also possible for active bodies at large heliocentric distances. Pockets of amorphous ice are formed at a low pressure and temperature from the process of rapid cooling or compression, such that that is no time to create a crystalline

arrangement in the process. It is theorized that all comets have amorphous ice in their interior, as comets were likely formed in the conditions described above (Mekler & Podolak [1994]). Species more volatile than water can also exist in gaseous form, trapped this amorphous water-ice matrix, which has been shown by laboratory experiments to be an efficient way to trap large amounts of volatiles (Bar-Nun et al. [1987]). When this amorphous ice crystallizes, it releases heat and the trapped volatiles in the process. The heat triggers additional crystallization in surrounding areas leading to a runaway effect (the peak temperature for this being 120–130 K, or within 10 au), which could be a potential trigger for a sublimation outburst (Prialnik et al. [2004]).

Until recently, scientists have not had a chance to thoroughly explore CO- or CO_2-driven activity, in part because previous surveys did not discover objects approaching perihelion far enough out to see them before they turned on, and in part because CO-rich comets are relatively rare (Meech et al. [2017]). Fortunately, over the past decade, the University of Hawai'i has led the way in characterizing faint primitive body discoveries and follow-up observations using various telescopes and deep surveys. These include the Canada–France–Hawaii Telescope (CFHT) Ecliptic Plane Survey (CFEPS; Jones et al. [2006]), the Pan-STARRS all-sky survey (PS1; Chambers et al. [2016]), the Asteroid Terrestrial-impact Last Alert System (ATLAS; Tonry et al. [2018]), and, in the future, the All-Sky Automated Survey for Supernovae (Shappee et al. [2014]) adapted for near-Earth objects (Shappee, private communication).

This explosion of deep all-sky surveys is currently creating a new avenue to probe solar system models with efficient detection and orbit characterization of faint objects. This gives us the opportunity to examine the volatiles over a much larger range of object types at a wider range of distances than before.

On 2009 June 25, 2009 MS9 (asteroid 418993) was discovered using the CFHT as a part of the High Ecliptic Latitude extension of the CFEPS (Petit et al. [2017]). It was found at a distance of 12.9 au from the Sun and an ecliptic latitude of 71° (Petit et al. [2017]) and classified as an exotic trans-Neptunian object (TNO) because of its highly eccentric ($e \sim 0.97$) and inclined ($i \sim 68°$) orbit and its large semimajor axis ($a \sim 388$ au) at epoch JD = 2,459,600.5. Additionally, 2009 MS9 was identified in the PS1 survey of outer solar system objects as a distant solar object with one of the highest inclinations in the survey, with a maximum brightness $V_{max} > 20.0$, which is considered bright for a minor body with such a large perihelion distance ($q = 10.99$ au; Weryk et al. [2016]).

Petit et al. ([2017]) obtained photometry of 2009 MS9 from 2009 to 2011. They conducted follow-up Palomar observations of the object in 2009 August and determined a single-peaked rotation period of ~6.5 hr, or 13 hr double-peaked, with a maximum magnitude change of 0.4 mag (Petit et al. [2017]). Additional *BRV* colors were reported by Jewitt ([2015]) in their survey investigating the colors of comets and related bodies.

Publicly available photometry of 2009 MS9 compiled through the Multitudinous Image-based Sky-survey and Accumulative Observations (MISAO) project,[9] which gathers Minor Planet Center (MPC) data (reported values of amateur and professional observations from various observatories), showed that near 2009 MS9's perihelion at $Q = 10.99$ au on 2013 February 14, the data did not seem to be following the
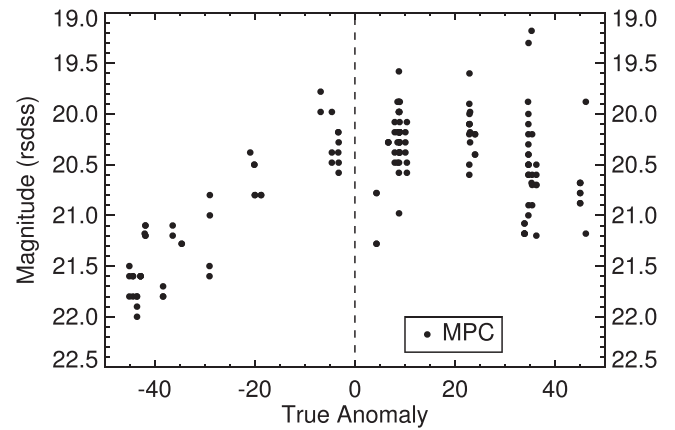
---
[9] http://www.aerith.net/misao/index.html

Figure 1. Heliocentric light curve of 2009 MS9 shown with data from the MPC, which consists primarily of photometry from various sources, including amateur telescopes. The asymmetry of brightening post-perihelion is suggestive of activity.

brightness variations expected for an asteroid; that is, the target experienced brightening post-perihelion, suggesting possible activity (see Figure 1). Research has shown that many long-period comets (LPCs) can become active around 10 au (Meech et al. [2009]); this is very similar to the perihelion of 2009 MS9 ($q \sim 10.99$ au). Although officially classified as a TNO, because of this and its unique orbital properties, 2009 MS9 has been described as a Damocloid (Jewitt [2015]; probable inactive LPC) and a Manx candidate (object on a LPC orbit with minimal activity and potential inner solar system origins; Meech et al. [2016]).

While there has been research investigating TNO activity (Meech et al. [2003]), and certainly such activity would be one explanation for the diversity of TNO and Centaur colors (Hainaut et al. [2000]; Sekiguchi et al. [2002]; Meech et al. [2003]), there has been no direct evidence for sublimation to date (Young et al. [2020]), with the exception of the dwarf planet Pluto (Gladstone & Young [2019]). Hence, if 2009 MS9 is found to have volatile activity, this would the first detection of its kind.

In this paper, we attempt to verify volatile activity in 2009 MS9 using the following methods:

1. using the heliocentric light-curve photometry to compare this to a nucleus plus volatile activity light curve with an ice sublimation model;
2. creating composite images to visually search for a coma quantified with a comparison of 2009 MS9 and stellar radial profile fluxes; and
3. analyzing colors pre- and post-perihelion to search for changes caused by activity-driven removal of surface materials.

We use an ensemble of photometric measurements taken from data obtained from several facilities, including multiple observatories on Maunakea. We describe the observations in detail in Section 2 below.

2. Observations

The geometry of all of the observations is detailed in Table 1. We processed all of the ground-based CCD imaging data using the same technique and tools as described in Meech et al. ([2017]); we use the Terapix/Astromatic tools

Table 1
Observing Geometry and Photometry

UT Date	JD[a]	r[b]	Δ[b]	α[b]	TA[c]	Filt.	No. Images	mag $\pm \sigma$	$r_{mag} \pm \sigma$[d]	Color/Comment
PS1 Data										
2010/06/04	5,352.10123	28.665	28.754	2.017	−151.16	i_{p1}	2	<21.0 ± 0.3	<21.2 ± 0.3	Limiting mag
2012/08/07	6,146.81325	25.061	25.146	2.306	−149.01	r_{p1}	2	<21.8 ± 0.3	<21.8 ± 0.3	Limiting mag
2014/06/14	6,821.46247	21.802	21.829	2.666	−146.54	i_{p1}	3	<21.0 ± 0.3	<21.2 ± 0.3	Limiting mag
2014/06/13	6,822.51886	21.797	21.824	2.667	−146.54	i_{p1}	3	<20.7 ± 0.3	<20.9 ± 0.3	Limiting mag
2014/07/05	6,844.27742	21.688	21.729	2.681	−146.45	i_{p1}	2	<20.8 ± 0.3	<21.0 ± 0.3	Limiting mag
2014/03/20	6,737.07683	22.221	22.202	2.569	−146.88	r_{p1}	2	20.67 ± 0.30	20.67 ± 0.30	
2014/09/08	6,908.76850	21.364	21.430	2.692	−146.17	i_{p1}	4	20.60 ± 0.05	20.77 ± 0.05	
2015/05/06	7,149.01152	20.138	20.122	2.871	−145.09	i_{p1}	4	20.10 ± 0.04	20.28 ± 0.04	
2015/05/07	7,150.00904	20.133	20.117	2.872	−145.08	i_{p1}	4	20.27 ± 0.05	20.45 ± 0.05	
2016/05/27	7,536.02124	18.088	18.052	3.211	−143.07	r_{p1}	4	19.53 ± 0.04	19.53 ± 0.04	
2016/06/19	7,558.88673	17.963	17.938	3.242	−142.94	i_{p1}	3	19.37 ± 0.08	19.54 ± 0.08	
2016/06/21	7,560.93624	17.952	17.928	3.245	−142.93	i_{p1}	2	19.37 ± 0.06	19.54 ± 0.06	
2016/07/18	7,587.88946	17.805	17.803	3.270	−142.77	i_{p1}	4	19.53 ± 0.05	19.71 ± 0.05	
2017/04/10	7,854.05173	16.322	16.280	3.519	−141.06	i_{p1}	4	19.19 ± 0.07	19.36 ± 0.07	
2017/05/21	7,894.91140	16.089	16.019	3.604	−140.77	w_{p1}	4	19.45 ± 0.03	19.39 ± 0.03	Discovery
2017/06/16	7,920.97821	15.940	15.874	3.651	−140.59	i_{p1}	4	18.85 ± 0.04	19.02 ± 0.04	
2017/06/25	7,929.91675	15.888	15.828	3.666	−140.52	w_{p1}	4	19.19 ± 0.03	19.13 ± 0.03	
2017/08/06	7,971.88255	15.646	15.638	3.715	−140.21	i_{p1}	4	18.94 ± 0.05	19.11 ± 0.05	
2017/08/17	7,982.77565	15.583	15.594	3.721	−140.13	w_{p1}	4	19.02 ± 0.01	18.97 ± 0.02	
2017/08/30	7,995.76736	15.508	15.542	3.725	−140.03	i_{p1}	4	18.78 ± 0.04	18.96 ± 0.04	
2017/09/07	8,003.77876	15.461	15.511	3.724	−139.96	i_{p1}	4	18.72 ± 0.04	18.90 ± 0.04	
2017/06/16	7,920.95557	15.940	15.874	3.651	−140.59	r_{p1}	4	18.96 ± 0.06	19.14 ± 0.06	
2017/07/05	7,939.88379	15.831	15.779	3.681	−140.45	r_{p1}	2	18.94 ± 0.14	19.11 ± 0.14	
2017/07/07	7,941.90196	15.819	15.770	3.684	−140.43	r_{p1}	4	19.24 ± 0.11	19.41 ± 0.11	
2017/07/15	7,949.87944	15.773	15.733	3.694	−140.37	r_{p1}	4	18.82 ± 0.06	19.00 ± 0.06	
2017/07/17	7,951.90526	15.762	15.724	3.696	−140.36	r_{p1}	4	19.15 ± 0.20	19.33 ± 0.20	
CFHT Archival Data from CADC										
2013/05/12	6,424.61132	23.744	23.767	2.436	−148.07	u	7	23.09 ± 0.17	20.76 ± 0.23	
CFHT New Data										
2017/05/24	7,898.05595	16.071	16.000	3.610	−140.75	w	1	19.292 ± 0.007	19.237 ± 0.007	
2017/05/28	7,901.92345	16.049	15.978	3.617	−140.72	g	1	19.673 ± 0.015		
2017/05/28	7,901.92345	16.049	15.978	3.617	−140.72	r	1	19.155 ± 0.015	19.155 ± 0.015	$(g − r) = 0.52 ± 0.02$
2017/06/24	7,928.97060	15.894	15.833	3.665	−140.53	g	1	19.539 ± 0.012		
2017/06/24	7,928.97049	15.894	15.833	3.665	−140.53	r	1	19.067 ± 0.013	19.067 ± 0.013	$(g − r) = 0.47 ± 0.02$
2017/07/16	7,950.83854	15.768	15.729	3.695	−140.37	r	12	19.081 ± 0.004	19.081 ± 0.004	
2017/07/25	7,990.80063	15.768	15.729	3.695	−140.37	g	1	19.567 ± 0.011		$(g − r) = 0.56 ± 0.02$
2017/07/25	7,990.80285	15.768	15.729	3.695	−140.37	r	1	19.007 ± 0.012	19.007 ± 0.012	
2017/07/26	7,991.80022	15.537	15.562	3.724	−140.06	u	2	21.260 ± 0.054		$(u − r) = 2.33 ± 0.06$
2017/07/26	7,991.80602	15.531	15.558	3.724	−140.06	g	1	19.513 ± 0.013		$(g − r) = 0.59 ± 0.02$
2017/07/26	7,991.80407	15.537	15.562	3.724	−140.06	r	3	18.927 ± 0.008	18.927 ± 0.008	
2017/07/26	7,991.80889	15.531	15.558	3.724	−140.06	i	2	18.758 ± 0.013		$(r − i) = 0.17 ± 0.02$
2017/09/14	8,010.74649	15.421	15.483	3.723	−139.91	g	4	19.483 ± 0.005		$(g − r) = 0.55 ± 0.01$
2017/09/14	8,010.74282	15.421	15.483	3.723	−139.91	r	2	18.932 ± 0.009	18.932 ± 0.009	
2017/09/14	8,010.74230	15.421	15.483	3.723	−139.91	i	6	18.761 ± 0.008		$(r − i) = 0.17 ± 0.01$
2017/09/14	8,010.75793	15.421	15.483	3.723	−139.91	z	4	18.721 ± 0.024		$(r − z) = 0.21 ± 0.03$
2017/09/15	8,011.72479	15.415	15.479	3.723	−139.90	u	3	20.995 ± 0.039		$(u − r) = 2.12 ± 0.04$
2017/09/15	8,011.74031	15.415	15.479	3.723	−139.90	g	5	19.413 ± 0.004		$(g − r) = 0.54 ± 0.01$
2017/09/15	8,011.75514	15.415	15.479	3.723	−139.90	r	2	18.873 ± 0.007	18.873 ± 0.007	

Notes.
[a] Julian Date −2,450,000.0.
[b] Heliocentric, geocentric distance (au) and phase angle (deg).
[c] True anomaly (deg), position along orbit, TA at perihelion = 0°.
[d] Magnitude and error through 5″ radius aperture.
[e] Magnitude and error converted to SDSS r as described in the text.

(Bertin & Arnouts 1996) to fit world coordinates (R.A. and decl.) based on reference stars from the 2MASS catalog. We used SExtractor (Bertin & Arnouts 1996) automatic apertures to measure the magnitudes of trailed stars and computed a photometric zero-point for each image based on stars from the PS1 database (Flewelling et al. 2020; Magnier et al. 2020) 3π

Steradian Survey (Chambers et al. 2016). Lastly, we used the Terapix tool (SExtractor) to produce multiaperture target photometry. We visually inspected each image and removed those contaminated by background objects, bad pixels, or cosmic rays. We used a $4''$ aperture for photometry, as that yielded the most uncontaminated images for analysis, as many of our observations were in crowded fields.

We convert all of our magnitudes to the Sloan Digital Sky Survey (SDSS) r filter shown in Table 1 using the following filter transformations.

From R Cousins system magnitudes to r, we used the transformations of Lupton (2005):

$$r = R + 0.183\ 7(g - r) + 0.0971$$
$$\sigma_r = \sigma_R^2 + (0.1837\sigma_{(g-r)})^2 + 0.0106^2. \quad (1)$$

The transformations from the PS1 filters to r are given by Tonry et al. (2012):

$$r = g_{P1} + 0.011 - 0.875(g - r) + 0.015$$
$$(g - r)^2, \sigma_r = (0.006^2 + \sigma_{gp1}^2)^{0.5}, \quad (2)$$

$$r = r_{P1} - 0.001 + 0.006(g - r) + 0.002(g - r)^2,$$
$$\sigma_r = (0.002^2 + \sigma_{rp1}^2)^{0.5}, \quad (3)$$

$$r = i_{P1} + (r - i) - 0.004 + 0.014(g - r)$$
$$- 0.001(g - r)^2, \sigma_r = (0.003^2 + \sigma_{ip1}^2)^{0.5}, \quad (4)$$

$$r = z_{P1} + (r - z) + 0.013 - 0.040(g - r)$$
$$+ 0.001(g - r)^2 \sigma_r = (0.009^2 + \sigma_{zp1}^2)^{0.5}, \quad (5)$$

$$r = w_{P1} - 0.018 - 0.118(g - r) + 0.091(g - r)^2$$
$$\sigma_r = (0.012^2 + \sigma_{wp1}^2)^{0.5}. \quad (6)$$

We report on the average magnitude for nights where multiple images in the same filter are taken, and these magnitudes are used to construct the target's heliocentric light curve (see Section 3.5). Color corrections for each R observation are made based on the target's Gemini or CFHT colors (e.g., $g - r$) closest to when the data were taken.

2.1. CFHT

Data were obtained from the Canada–France–Hawaii Mega-Cam wide-field imager, an array of 40 2048×4612 pixel CCDs with a plate scale of $0''187$ pixel^{-1} and a 1.1 deg^2 field of view. Petit et al. (2017) obtained 636 observations of 2009 MS9 over 40 nights between 2009 June 25 and 2016 February 6 as follow-up photometry to the 2009 June discovery. Additionally, in 2010 July and October, several nights of gri magnitudes were obtained pre-perihelion (Petit et al. 2017). Our team also obtained photometry with MegaCam during 2014, 2017, 2018, 2020, and 2021.

2.2. Gemini Observatory

Photometric observations of 2009 MS9 were taken on six nights between 2015 and 2021, and $griz$ or $griZY$ colors were obtained on four of those dates. Data were obtained from the Gemini North 8 m telescope on Maunakea or the Gemini South 8 m telescope with the Gemini Multi-Object Spectrograph (GMOS; Hook et al. 2004) in imaging mode. GMOS is a mosaic of three 2048×4176 Hamamatsu detectors binned 2×2. The data were obtained through SDSS filters using

queue service observing and processed to remove the instrumental signature using DRAGONS, Gemini Observatory's Python-based data reduction software (Labrie et al. 2019). For nights where the outer chips were nonphotometric due to guide probe vignetting, we extracted only the central chip of the mosaic so that the zero-point calibration would not be affected.

2.3. Lowell 1.8 m Perkins Telescope

Data were obtained during 2013 October 4 and 5 using the 1.8 m Perkins telescope at Lowell Observatory with the Perkins ReImaging SysteM (PRISM) in imaging mode. The $2 \times$ K E2V CCD has $0''39$ pixels with a gain of 2.72 e^- ADU^{-1} and read noise 7.2 e^-. The data were guided at nonsidereal rates under photometric conditions but with mediocre seeing ($2''0$ FWHM) on both nights.

2.4. Himalayan Chandra Telescope

As part of our Manx characterization efforts, we have a long-term program on the 2.01 m Himalayan Chandra Telescope (HCT) at Mt. Saraswati, Hanle, India, to obtain images for astrometry and heliocentric light curves. We used the Himalaya Faint Object Spectrograph and Camera with the Bessell/Cousins filter system to obtain data on the two dates shown in Table 1. The detector has a read noise of 4.8 e^- and gain of 1.22 e^- ADU^{-1} and was read out in 1×1 binning mode with a pixel scale of $0''296$ pixel^{-1}. This telescope cannot autoguide at nonsidereal rates, so we kept the exposures short enough to keep trailing to less than the typical seeing while guiding at sidereal rates.

2.5. NEOWISE

The NEOWISE mission uses the reactivated Wide-field Infrared Survey Explorer (WISE) spacecraft, which began survey operations in 2013 December (Mainzer et al. 2014). Without any cryogens, only the two short-wavelength channels at 3.4 (W1) and 4.6 (W2) μm are available. Thirty-four exposures of 2009 MS9 were obtained between 2010 May 21 and 23 (mid-obs. time 2010-05-22T20:07:27.597) for a total exposure time of 300 s.

2.6. PS1

The PS1 astrometric positions of 2009 MS9 were identified by the Moving Object Processing Pipeline (Denneau et al. 2013), and photometry was extracted using the Pan-STARRS Image Processing Pipeline (Magnier et al. 2020). Pan-STARRS photometry was provided in the g_{P1}, r_{P1}, and i_{P1} Pan-STARRS filters by point-spread function (PSF) photometry in ubercalibrated chip-stage images (Schlafly et al. 2012) with associated measurement uncertainties.

3. Data Analysis

3.1. WISE Nucleus Size Modeling

The WISE data were processed through the WISE science data pipeline (Wright et al. 2010) to bias subtract, flatten the images, and remove artifacts. The 34 images are then stacked using the comet's apparent rate of motion. In order to produce a spectral energy distribution, aperture photometry is converted to fluxes using the WISE zero-points and appropriate color

temperature corrections (Wright et al. 2010). These corrections are temperature-dependent, and an initial guess at the temperature is required based on the expected blackbody temperature for the heliocentric distance of the observation. The data were acquired during the warm mission, and we use a technique that has been modified by Reach et al. (2013) for the Spitzer warm mission to work with only the two shortest-wavelength bands, W1 and W2. We measure the flux of 2009 MS9 from the image; then, the size of the target is measured with this flux in combination with a thermal model.

Initially, Lebofsky et al. (1986) developed the standard thermal model to determine the thermal flux of inactive minor bodies. This model uses a target's orbital properties and optical/thermal phase coefficients and is quantified by a "beaming parameter." The beaming parameter accounts for the difference between isotropic and nonisotropic thermal emission of minor bodies in the infrared. The near-Earth asteroid thermal model (NEATM) arose from allowing the thermal phase coefficient of the target to vary as a free parameter that can be fit when two or more infrared bands are available (Harris 1998). Wright (2007) found that in comparison to a more sophisticated thermal model, the NEATM and associated beaming parameter give diameters that are accurate to within 10%. For Jupiter-family comets and outer solar system objects, the average beaming parameter was measured to be 1.03 ± 0.11 and 1.2 ± 0.35 (Stansberry et al. 2008; Fernández et al. 2013). We use the NEATM and determine the beaming parameter using a least-squares minimization in comparison to the WISE detections (Mainzer et al. 2011). This yields a beaming parameter of 0.95 ± 0.3 (Bauer et al. 2015) and a resulting radius of $R_N = 11.5 \pm 3.5$ km. Using this radius, we can combine this with the MPC's absolute magnitude of $H = 9.8$ and use the traditional relationship between absolute magnitude (H), nucleus diameter (D), and geometric albedo (p) to recover p:

$$D = \frac{1329}{\sqrt{p}} 10^{-0.2H}.$$ (7)

This yields an estimated albedo of $p = 0.40 \pm 0.14$. However, because the H values reported by the MPC are not always accurate, we independently derive the albedo for 2009 MS9 in Section 3.4.

3.2. Composite Images

Deep composite images are powerful tools for detecting weak activity that may not be apparent in individual images. This is especially important for characterizing activity in comets where a dust tail is not immediately apparent. We thus create composite images of 2009 MS9 at several epochs in an attempt to detect activity and/or place limits on activity in its orbit in the event none is detected. Because this object has data that span over a decade, we use Finson–Probstein (FP) plots, exposure time, our object's orbital position, and telescope capabilities to evaluate which observations are the most likely to yield dust from composite images.

The FP plots (Finson & Probstein 1968) represent the trajectories of dust emitted from the nucleus of an active body at a specific time of its orbit, governed by the forces of solar radiation pressure and gravity. They consist of synchrones (lines of constant time) and syndynes (lines of constant grain sizes) to map out a target's expected dust tail map, assuming the emission velocities of the dust are negligible. Thus, an FP

plot, while not exact, is a good approximation of the expected behavior of the tail for a given position in a comet's orbit.

We can use FP plots to our advantage to strategically pick out observations where the signal-to-noise ratio (S/N) of the dust tail will be maximized. A nonfavorable viewing geometry is when the dust is spread out over a larger region of the sky and thus the surface brightness of the comet tail is lower (i.e., Figure 2, top panel). The detection of dust is most likely when an active body has a tail that is edge-on to the observer (i.e., Figure 2, bottom panel). This is when the dust is concentrated in the plan of the dust emission (the comet's orbital plane); thus, the S/N is high because the synchrones and syndynes will gather over a smaller area of the sky. Keeping this in mind, we generate FP diagrams to map out the positions of dust grains for active bodies in the solar system.

The deeper the composite (e.g., the longer the effective exposure time), the more likely we are to be able to detect dust from activity. Hence, we also choose observations taken with large-aperture telescopes on nights with the most images, giving the longest exposures. Next, we selected observations close to perihelion, where the input of energy is the greatest, which would translate to a larger gas/dust production rate, and post-perihelion, where 2009 MS9 is most likely to become active following a delayed outburst of activity (see Section 3.4 for further discussion of this). Our inspection of 2009 MS9's photometric data shows that the largest deviation from the fit nucleus light curve occurs most prominently post-perihelion, after TA ~ 20 (see Figure 6).

The list of observations we have created composite images for, as well as their observing circumstances and the target's orbital properties, is given in Table 2, with the dust viewing conditions quantified as good, fair, or bad by the predicted level of concentration of dust near the orbital plane as estimated by the FP plots. The seventh and eighth columns from Table 2 result from this paper's modeling and are discussed in further detail in Section 3.3.

The creation of composite images requires several steps of data reduction to accurately prepare the images in an attempt to detect comet dust in a faint target. First, we flag and remove single images where 2009 MS9 overlaps a background object, bad pixel, or cosmic ray. Next, we "superflatten" each image using SExtractor to approximate and subtract the shape and amplitude of the background for each observation such that the background is approximately zero. Accurate subtraction of the background is critical. Because of this, we iterate through different values of SExtractor's background parameters "BACK_SIZE" and "BACK_FILTER" until the flatness of the background is optimized. If BACK_SIZE and/or _FILTER have values that are too small, this will interfere with the wings of bright stars and risks subtraction of a potential coma surrounding 2009 MS9. Because of this, we take care to manually inspect the values of BACK_SIZE and _FILTER for each composite image, and the value of BACK_SIZE does not go under 84 pixels in diameter. We then apply a bad-pixel mask to each image to get rid of persistent artifacts, bad pixels, or cosmic rays. For each night, we align the images to the PS1 reference stars used for calibration to compensate for dithering. An example of a single reduced image is shown in Figure 3(a).

We median combine the images to create a star template for subtraction (Figure 3(b)). As the PSF of MS9 is often larger than the apparent velocity of the object and time elapsed between observations, a relic of 2009 MS9 is still prevalent in
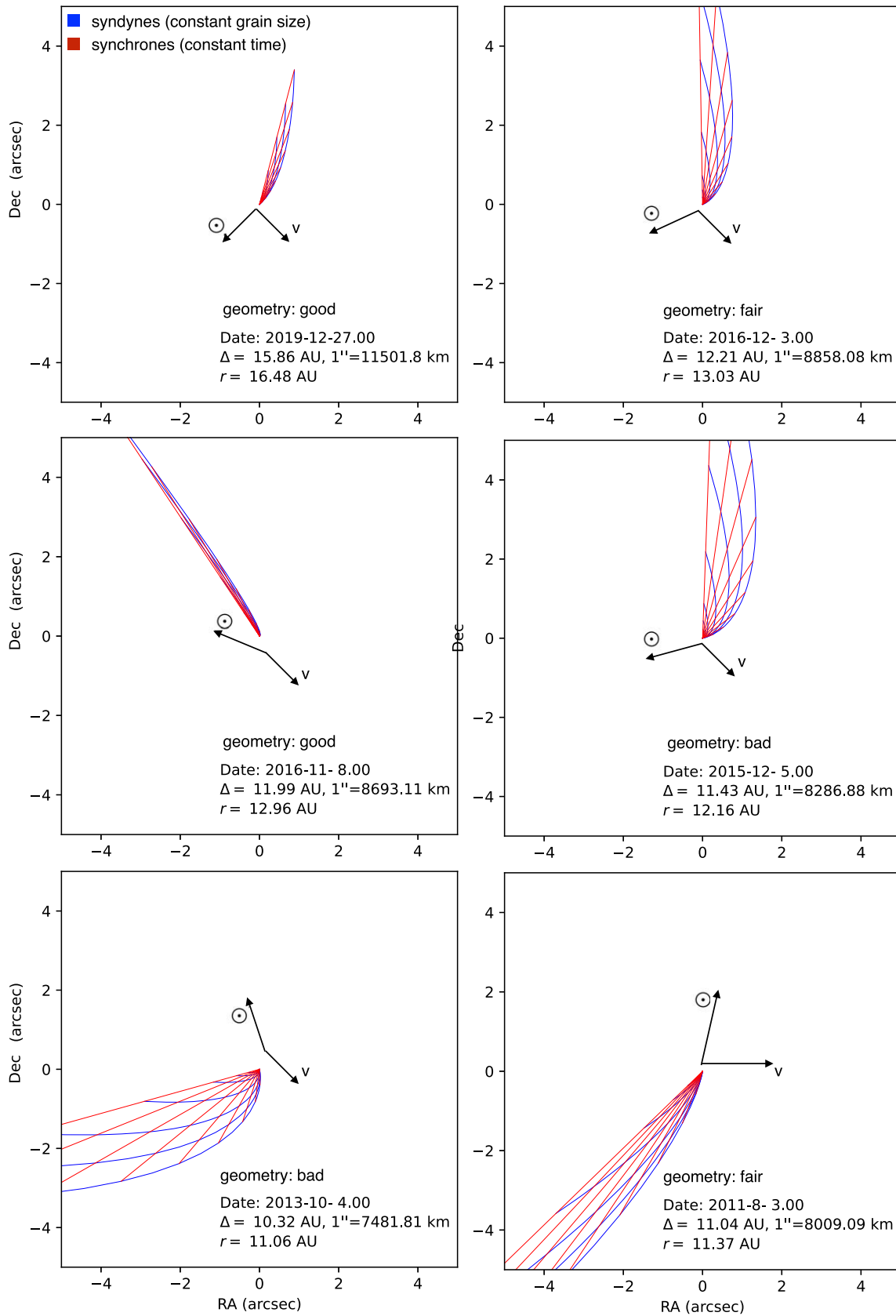
Figure 2. The FP modeling of the dust for 2009 MS9 for different epochs. Each panel is labeled with the viewing geometry quality (bad, fair, or good). Bad quality represents when the viewing geometry is far from the plane of the orbit. Good quality represents when the viewing geometry is close to the orbital plane. For the latter, dust is more likely to be detected because the synchrones and syndynes are concentrated and overlap in a smaller area.

Table 2
Composite Images and Dust Limits

No.	Date	Obs.	Exp. (tot)	Dust View	TA (deg)	r (au)	Dust Limit (kg s^{-1})			Predicted Dust (kg s^{-1})		
							0.5 μm	2 μm	10 μm	0.5 μm	2 μm	10 μm
1	8/19–21 2009	CFHT	6500	Fair	−44	12.74	$0.022^{+0.007}_{-0.007}$	$0.088^{+0.028}_{-0.027}$	$0.441^{+0.138}_{-0.133}$	0.015	0.059	0.355
2	9/11 2010	CFHT	6250	Bad	−32	11.88	$0.021^{+0.009}_{-0.006}$	$0.085^{+0.035}_{-0.025}$	$0.425^{+0.176}_{-0.124}$	0.018	0.069	0.411
3	7/31–8/1 2011	CFHT	6000	Fair	−21	11.37	$0.040^{+0.042}_{-0.016}$	$0.159^{+0.169}_{-0.063}$	$0.794^{+0.730}_{-0.316}$	0.020	0.075	0.450
4	8/2–3 2011	CFHT	6000	Fair	−21	11.37	$0.031^{+0.042}_{-0.011}$	$0.123^{+0.080}_{-0.045}$	$0.616^{+0.402}_{-0.223}$	0.020	0.075	0.450
5	10/4 2013	Lowell	8100	Bad	9	11.07	$0.009^{+0.002}_{-0.003}$	$0.035^{+0.006}_{-0.010}$	$0.177^{+0.030}_{-0.052}$	0.021	0.079	0.477
6	9/8 2015	Gemini	800	Fair	33	11.98	$0.032^{+0.027}_{-0.014}$	$0.127^{+0.106}_{-0.056}$	$0.633^{+0.532}_{-0.280}$	0.018	0.068	0.408
7	12/4–5 2015	HCT	4500	Bad	36	12.16	$0.028^{+0.012}_{-0.007}$	$0.111^{+0.047}_{-0.026}$	$0.554^{+0.233}_{-0.130}$	0.017	0.066	0.395
8	11/8 2016	Gemini	900	Good	46	12.96	$0.014^{+0.011}_{-0.005}$	$0.057^{+0.044}_{-0.021}$	$0.283^{+0.220}_{-0.104}$	0.015	0.058	0.347
9	12/3 2016	HCT	2700	Fair	46	13.03	$0.054^{+0.048}_{-0.019}$	$0.218^{+0.048}_{-0.077}$	$1.09^{+0.239}_{-0.384}$	0.015	0.057	0.347
10	12/27 2019	Gemini	3000	Good	71	16.48	$0.021^{+0.009}_{-0.010}$	$0.084^{+0.034}_{-0.040}$	$0.421^{+0.172}_{-0.200}$	0.009	0.035	0.212
11	2/20 2020	Gemini	1000	Good	72	16.66	$0.025^{+0.077}_{-0.009}$	$0.099^{+0.306}_{-0.034}$	$0.494^{+1.53}_{-0.170}$	0.009	0.035	0.207

Note. Dates and observing circumstances for which we have created composite images of 2009 MS9. The table is split into pre- and post-perihelion observations separated by a double horizontal lines. "Dust view" refers to whether or not the object is observed with a predicted dust tail close to the plane (see Figure 2 for reference). The dates that yield the most favorable circumstances for detecting dust are denoted as good, with less favorable circumstances denoted as fair and bad. Numbers after each date correspond to the radial profiles shown in Figure 4 (see text). The last two columns show the dust limits at the background limit from each composite's azimuthally averaged profiles in comparison to the dust production rate from sublimation modeling assuming a 1–1 gas-to-dust ratio.
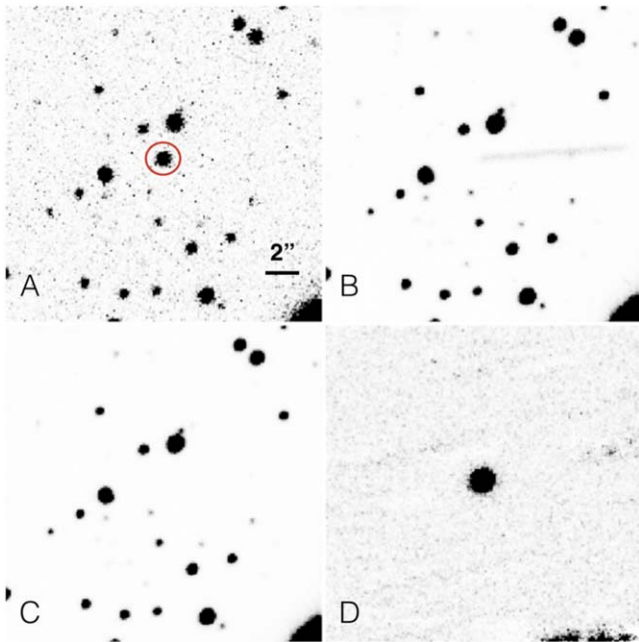

Figure 3. Process of creating a composite *r*-band image of 2009 MS9 using 45 images from CFHT obtained on 2011 July 31. (a) One frame with an exposure time of 120 s, where 2009 MS9 is highlighted by red circle. (b) Sum composite image, where 2009 MS9 is seen as trailed. (c) Star template from a median composite image for the night of 2011 July 31, which is used for stellar radial profiles and subtraction. (d) Average composite image shifted by the KBO apparent rate of motion or 2009 MS9's astrometric position per night.

star templates. We alleviate this issue by manually replacing the minor body with simulated background noise using routines in IRAF for several images in one night's stack (Figure 3(c)). We then subtract the star template from each image and then shift each image according to 2009 MS9's apparent rate of motion or astrometric position.

We median combine the 2009 MS9–shifted images to create the final composite stack with just 2009 MS9 in the observation (Figure 3(d)). If there are several consecutive nights, we

execute the above process for each individual night and lastly align each night's 2009 MS9 composite with astrometrically calculated positions to create the final stack.

Nearly half of our composites were created manually, while the rest were created using an automated version of the above methods with the use of SWARP (Bertin 2010) for the image shifts and stacking and an automated SExtractor background subtraction built into the routine. We create 11 stacks total at different epochs or positions along 2009 MS9's orbit. We do not visually detect dust in any of our composite images. However, this can be quantified with an analysis comparing the flux profile of 2009 MS9 with those of field stars, and this is used to calculate a limit on the dust production, as is discussed in detail below.

3.3. Dust Modeling

While a deep composite image can provide visual confirmation of a dust coma, this property can be qualified by inspection of 2009 MS9's radial brightness profile in comparison to the average stellar profile of stars created from a star template. The deviation of 2009 MS9 from the stellar profile will yield sensitive limits on the amount of dust at that given epoch.

A comet with no detectable coma will have a near-identical azimuthally averaged radial profile to stars in the same field, with an associated error. This error can be used to determine the upper limit on dust production or the maximum flux contribution from scattered coma light (Meech et al. 2003). We use 3σ to define this upper limit. This flux, F, is related to the dust production rate Q_p s^{-1} by

$$F = S_\odot \pi a_{gr}^2 p_v Q_p \phi / 2r^2 \Delta^2 v_{gr}, \qquad (8)$$

where $S_\odot$ is the solar flux in the appropriate filter, a_{gr} is the average grain size, p_v is the grain albedo, ϕ is the projected diameter of the aperture (m), r and Δ are the heliocentric and geocentric distances, and v_{gr} is the grain velocity. The total dust production Q is then $Q_p \times$ grain mass.

We derive the flux from our surface brightness profiles. Using this, we can use Equation (8) to derive the dust production rate assuming a volatile species such as CO or CO_2. We can use this dust production rate to set limits on our sublimation modeling (see Section 3.5).

We construct the radial profiles of our target by measuring the target's flux in increasingly large apertures or annuli; the radius of each annulus increases by 1 pixel out to 30 pixels from the center, which encapsulates the target plus some background. We convert this to magnitudes per square arcsecond after photometrically calibrating the target image using the zero-point from the associated star template combined with the plate scale (arcseconds per pixel) unique to the telescope used for each composite image.

We then implement the same technique for two to five stars of comparable brightness in the star templates associated with each composite image and use this to create an average flux profile for the stars. We then compare this to the relative flux profile of 2009 MS9 to see if there is qualitative evidence of a coma.

To ensure that both our manual and automated methods produce consistent results, we implement both for our 2010 September and 2015 September composite images and compare. We find that both techniques yield radial profiles that are nearly identical and dust limits that deviate less than 0.05 kg s^{-1} from one another or by <5% around 1″ from the center of the profile. Hence, we are confident that our automated and manual methods of creating composites are consistent.

Each panel in Figure 4 represents the radial profile results for each composite image (11 total). This includes 2009 MS9's radial profile (black) in comparison to the average stellar profile (blue) and the resulting limit on dust production (red) using Equation (7). For reference, the seeing radius (or the FWHM radius) is shown with a black dashed line. Each panel also shows a "background limit" (gray dashed line), which is the radius at which the background begins to dominate the radial profile. The numbers correspond to the date of the composite image (first column of Table 2).

We find no quantitative detection of dust through our radial profiles; that is, 2009 MS9 does not deviate significantly from a stellar radial profile. Even though activity was not detected, we can still use the error on the radial profile of 2009 MS9 to provide upper limit estimates of the dust production. Using the techniques described above, we measure the dust limits from the composites pre- and post-perihelion for grain sizes of 0.5, 2, and 10 μm.

The maximum amount of dust we can detect is governed by where the background noise begins to dominate. We report the dust limit as the dust production rate where the surface brightness of the object is equal to the sky noise (Table 2). The uncertainty in this observation is defined as the change in dust production ±1 pixel from this value.

3.4. Determining the Best-fit Albedo

Because of the uncertainty associated with the calculation of the H value from the MPC, we calculate our own estimate of the nucleus albedo using the radius obtained by WISE (11.5 km; Section 3.1) and photometric observations of 2009 MS9.

We compute the nucleus contribution to the photometry assuming a geometric albedo p and radius R, such that

$$pR^2 = 2.235 \times 10^{22} r^2 \Delta^2 10^{[0.4(m_\odot) - m]} 10^{0.4(\beta\alpha)}, \quad (9)$$

where r and Δ are the helio- and geocentric distances (au and $m_\odot$), and m is the apparent magnitude of the Sun and comet (Meech et al. 1986). The term β represents the simplified linear phase function with phase angle α (deg), and β is a constant ranging from 0.02 to 0.04 mag deg^{-1} (Meech et al. 1986). Thus, the main variables that affect the overall brightness of the asteroid light curve are the geometric albedo and size, and the rest come directly from the object's orbital geometry.

For 2009 MS9, because its perihelion is at 10.99 au, the likely driver for activity is either CO or CO_2. The CO ice can lift observable dust grains as far out as 25 au, and CO_2 ice sublimates inside of 12–13 au (Meech & Svoren 2004); this further depends on the evolution of the nucleus interior prior to the observed epoch. If we model the target as active throughout the entire duration of its orbit with typical CO or CO_2 sublimation (see Section 3.5), the WISE measurements on the nucleus size are just an upper limit. A simpler, equally likely explanation is to assume that 2009 MS9 is inactive pre-perihelion and active post-perihelion, and this time delay is caused by CO or CO_2 buried beneath the surface. For this scenario, fitting an asteroid curve to the observations pre-perihelion (e.g., for TA < 0°) will allow us to constrain the geometric albedo given the size of the target, which allows us to compare this to the calculated H value from the MPC. We do so while keeping in mind that the target's nucleus may indeed be an upper limit.

We use Equation (9) to calculate the nucleus light curve for varying albedos ranging from 0.15 to 0.40 in increments of 0.001. For each iteration, we calculate the sum of the residuals of the model from the observations, commonly known as the χ^2 statistic,

$$\chi^2 = \sum \frac{(x_i - \mu)^2}{\sigma_i^2}, \quad (10)$$

where x is the observed magnitude, μ is the expected magnitude from the asteroid model, and σ is the error on each observed magnitude. Our desire is to minimize the χ^2 statistic or weighted residuals so that we obtain the best-fit model to the observations.

If the model is a good fit to the data, we expect a χ^2 value approximately equal to our degrees of freedom, which is the difference between the number of observations and free parameters in the assumed model. Hence, the χ^2 statistic is redefined as χ^2/ν, or the reduced χ^2 statistic, where good fits have a reduced χ^2 value of ~1.

For our model and data, we have one free parameter and 29 observations before TA = 0°, which yields 28 degrees of freedom. To find the best-fit model, we need to minimize the weighted difference between the observations and what the model predicts. To do so, we need to also factor the 0.4 mag rotation (Petit et al. 2017) into the interpretation of our analysis; this is governing what we consider the best-fit model. This is much higher than any single observation's error; hence, taking the individual photometric errors into account, the reduced χ^2 statistic will be abnormally large. If we add the error associated with rotation to the photometric error, the χ^2/ν will be lower than expected because each data point will not necessarily
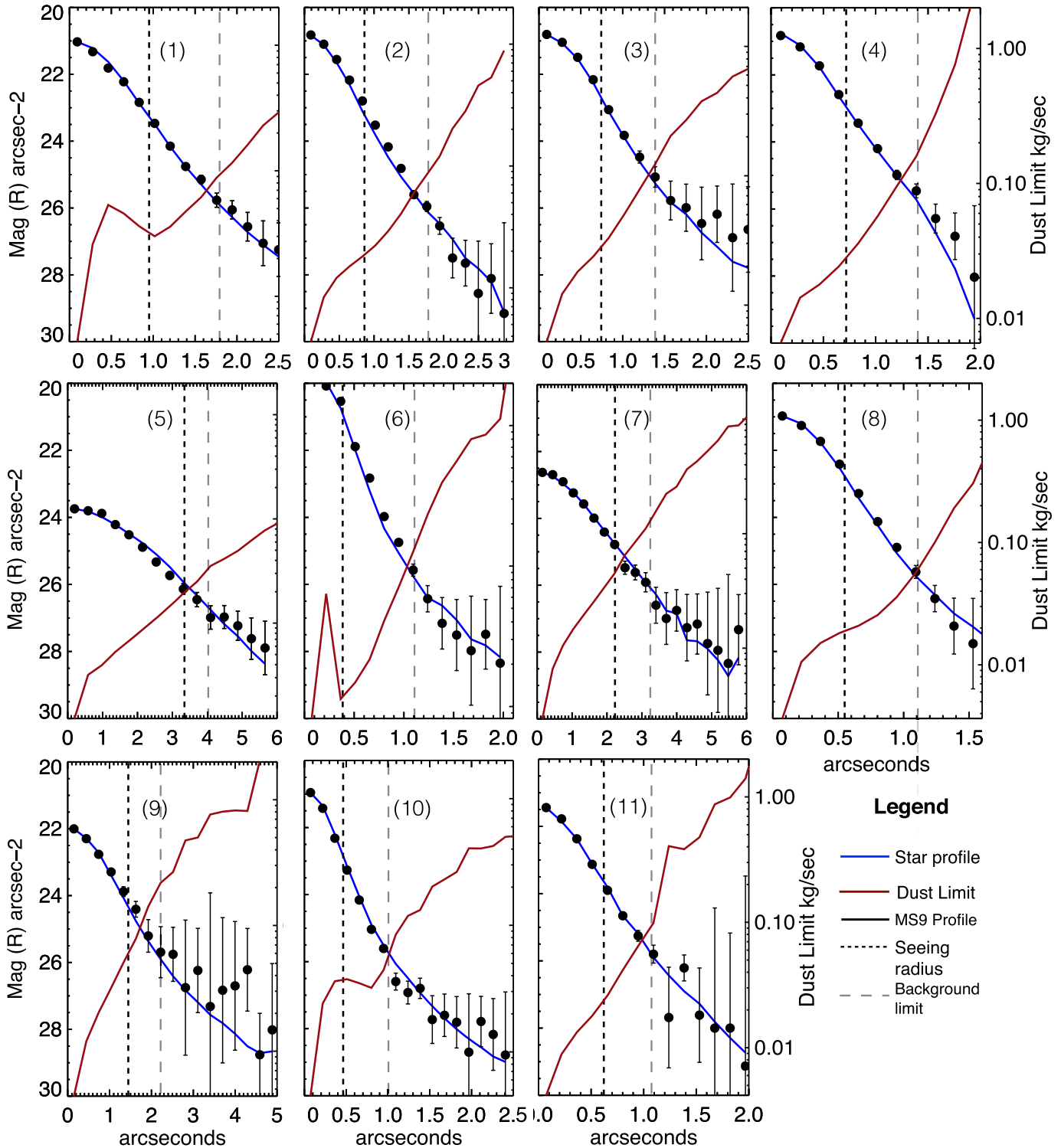
Figure 4. For each composite image, we bin the photon flux as a function of radius and calculate the average stellar radial profile of 2009 MS9 (black) vs. the average star profile (blue). From these profiles, we can calculate the limits on dust production (red).

contribute 1σ to the statistic as expected. Hence, the most valuable parameter for us is the weighted residual itself, minimized at a specific albedo. With this radius, the best-fit light curve to the data has an albedo of 0.25 ± 0.04, where the error is defined as the deviation from 0.25 at twice the weighted residual. Note that this is consistent with (although slightly lower than) the albedo and error calculated from the MPC H value, 0.4 ± 0.14.

3.5. Sublimation Modeling

We use an ice sublimation model that computes the amount of gas released due to solar heating and its overall effects on the object's heliocentric light curve (Meech et al. 1986; Meech & Svoren 2004). This ultimately results in an accurate prediction of gas loss and how the sublimation affects the object's brightness as it moves through its orbit (i.e., see

Table 3
Sublimation Model Parameters

Parameter	M1	M2	M3
Radius (km)	11.5	…	…
Emissivity, ϵ	0.9	…	…
Phase function (mag deg^{-1}), β_{nuc}	0.04	…	…
Phase function (mag deg^{-1}), β_{coma}	0.02	…	…
Grain density (kg m^{-3}), ρ_{grain}	1000	…	…
Nucleus density (kg m^{-3}), ρ_{nuc}	400	…	…
Albedo, p_v	0.25	…	…
Grain size (μm), a_{grain}	2	0.5	10
Log fract. active area (%), f_{CO}	−5.9	−5.3	−4.5

Snodgrass et al. 2013 for a comparison of this model to in situ gas flux measurements).

The sublimation light curve is produced using a fixed-aperture radius that combines the overall brightness from the nucleus with the coma, where the latter is produced by the gas sublimation and consequent drag of dust particles from the surface (Meech et al. 1986). We then compare the sublimation light curve to the photometric data to model the suspected activity for our target. There are 10 model free parameters that are involved: ice type, nucleus radius, albedo, emissivity, grain density, nucleus density, dust size, phase function, thermal conductivity, and fractional active area (FAA). Often, preliminary observations can reveal constraints on many of these parameters, allowing for an accurate prediction of the sublimation associated with the observed data with adjustments to only a few of the variables.

The FAA is the fraction of the cometary surface that is sublimating. Besides modeling, this value can be obtained by measuring a comet's total water production rate (from OH) and its radius (assuming that the nucleus is spherical; A'Hearn et al. 1995). Typical FAAs for comets with water-ice sublimation lie between 1% and 4% (A'Hearn et al. 1995). Much higher FAAs have been observed for targets with large, sublimating icy grains. An example of this is 103P/Hartley 2, which required over 100% of the comet's surface area to be actively sublimating (Groussin et al. 2004; Lisse et al. 2009). For hypervolatile species like CO and CO_2, FAAs are typically much lower than 1% (A'Hearn et al. 1995; Meech et al. 2017), although historically, this has been difficult to accurately assess. This is because LPCs with hypervolatiles often have unknown nucleus sizes due to being active at large distances. Manx comets, or objects on LPC orbits with unexpectedly low to no activity, have even lower FAAs; for example, 2013 LU28 is theorized to have an FAA of 10^{-4} and 10^{-6} for CO_2 and CO, respectively (Slemp et al. 2022), and A/2018 V3 has an FAA of 10^{-5} for water sublimation (Piro et al. 2021).

We assume typical cometary values for emissivity (Meech et al. 2017), nuclear and coma phase function (Krasnopol'Skii et al. 1987; Meech & Jewitt 1987), nucleus density (Thomas et al. 2013a, 2013b; Jorda et al. 2016), and grain parameters such as size and density based on both ground-based comet data and the Rosetta mission (Yang et al. 2014; Fulle et al. 2016). The distribution of grain sizes follows a power-law that describes how many 0.1 micron to mm grains exist in the dust tail. Usually the small particles are shown to dominate the emission (Fulle et al. 2016). Thus, for most models, we adopt an average grain size of 2 μm and vary this between submicron and 10 μm grains for selected CO models (see discussion below). The parameters are summarized in the first seven rows of Table 3. For this paper, our derived nucleus size and albedo were used to determine the FAA that best fits the photometric observations.

First, we explore the volatile species responsible for activity. Because of 2009 MS9's large perihelion, if it is active, it has CO and/or CO_2 sublimation. We investigate the expected light curve based on both CO and CO_2 models. We construct the heliocentric light curve with observations from professional telescopes, taking into account that the 0.4 mag rotation creates a range/envelope of possible brightnesses for any given date (Figure 5). Photometry is shown in SDSS r magnitudes, and we take the average of the observations taken on the same observing night. We plot the expected contribution of the nucleus using Equation (9) and the 0.4 mag rotation (gray shaded region) knowing the size to be 11.5 km and with the estimated 0.25 albedo.

We show three different models in Figure 5. The CO_2 modeling (top and middle panels) requires a changing FAA to explain the behavior post-perihelion. On the other hand, a CO model (bottom panel), while matching most data points, eventually deviates from the data past TA = 65. If we assume that CO is the dominating volatile species, then the comet activity stops beyond this. Activity dominated by CO or CO_2 is thus likely; however, for this paper, we adopt the simplest scenario, which is that 2009 MS9 has CO sublimation that is quenched past TA = 65.

Next, we investigate the duration of the suspected activity for 2009 MS9 with two CO models (Figure 6). In Section 3.4, we briefly mentioned the possibility that 2009 MS9 is active pre- and post-perihelion. If this is the case, then the measured diameter (gray shaded region) from WISE is an upper limit, and the target must have an outburst in activity post-perihelion (panel (a)). For this, we arbitrarily pick a nucleus size of 8 km and show that with 2 μm–sized grains, an FAA of 2.5×10^{-5} is needed pre-perihelion and 4×10^{-5} post-perihelion.

Figure 6(b) shows the best-fit model for only post-perihelion CO sublimation corresponding to an FAA of 5×10^{-6} that best fits the data post-perihelion up to TA = 65°, where the activity appears to cease.

From this point onward, we focus on the second scenario (Figure 6(b)), that 2009 MS9 was inactive pre-perihelion, and vary the grain sizes for our models. The TNO 2009 MS9 is far enough from the Sun that any ejected grain will have the same residence timescale around the nucleus. Therefore, it is useful to model 2009 MS9's activity assuming different dominating grain sizes. We thus report the CO model and resulting FAA with grain sizes of 0.5, 2, and 10 μm (Table 3).

The sublimation model with input FAA outputs the gas production rate. Using a 1:1 ratio of gas and dust, we can turn this into a dust production rate. Next, we have independently derived the limit on the dust production rate using Equation (8) and the surface brightness profiles of the composite images. This limit on the dust production value must be higher than the dust production predicted by sublimation; otherwise, we should be detecting the dust in the images. This is how the FAA can be constrained.

If we assume a 1:1 ratio of gas to dust from the sublimation model, the dust mass-loss rates (dm/dt) at the dates where we have dust limits from composites where we assume the target to be active are in the range 0.01–0.02, 0.04–0.08, and 0.2–0.5 kg s^{-1} from 2013 to 2019 for grain sizes of 0.5, 2, and 10 μm
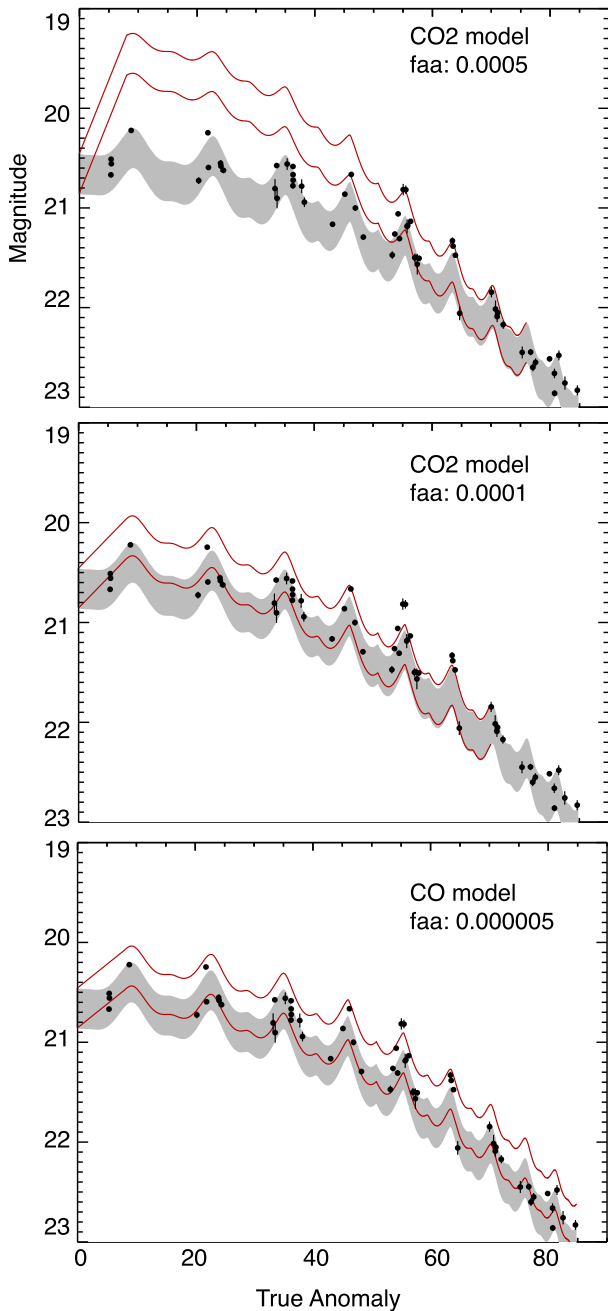
Figure 5. Three sublimation models showing how the light curve changes between volatile species CO and CO$_2$ in comparison to photometry. Top: CO$_2$ model matched to the brightnesses of the last data points of the target. Here the sublimation light curve does not match near-perihelion observations. Middle: CO$_2$ model matched to the initial photometry of the target. Observations after TA $= 50$ do not match the sublimation model. Bottom: CO sublimation matched to the photometry. This provides the best fit up to TA $= 65$; however, past this is too bright for observations.

(Table 2, "Predicted Dust"). For all of the surface brightness profiles except one, this is less than the upper limit on dust computed for each grain size. Thus, 2009 MS9 may be active post-perihelion, but the activity does not lift enough dust for a detectable coma in our composite images. The outlier surface brightness profile is from the composite image taken near perihelion on 2013 October 4, which has a more sensitive dust limit; this suggests that for 2 μm–sized grains, we should have detected activity. However, there are two factors that could

have affected this result: (1) the dust viewing geometry was poor (i.e., the dust was spread out over a larger area), and thus the dust may not have been concentrated enough for a high S/N for detection; and (2) since this data point is near perihelion (TA $= 8°$), the target may not have been active yet, as its photometry places these data just within the nucleus-only envelope.

In addition to the typical surface ice sublimation presented above, another driver of activity is the H$_2$O amorphous ice–to–crystalline ice transition. Amorphous water ice forms in low temperatures and traps gas from more volatile species in the process. When the ice anneals or undergoes a phase change to crystalline ice, this will release the trapped gas. Meech et al. (2009) showed that for a nonrotating body, the amorphous–crystalline phase change occurs between 120 and 160 K starting as far out as 11.5 au. For rapidly rotating isothermal bodies, this begins at much closer distances, inward of 7 au (Meech et al. 2009). Real comets are likely between these two cases. The perihelion of 2009 MS9 is 10.99 au, and it is a rotating body; therefore, it is likely too far out for the amorphous-to-crystalline ice transition to be the cause of activity. Whether or not ice annealing (which occurs as far out as 59 au for rapid rotators) could be a driver of activity could be explored in a future paper (Meech et al. 2009).

3.6. Thermal Modeling

The sublimation model described above accurately predicts the photometry produced by sublimation of volatiles at the surface; however, ice can be buried at a depth beneath the surface. This will result in a delay in the onset of activity depending on the thickness of the insulating layer, and modeling this requires a different technique. Object 2009 MS9 is predicted to have become active near its perihelion, at 10.99 au, which is at a closer heliocentric distance than would be expected for CO ice sublimation on the surface, which occurs as far out as 130 au, where the effective temperature at the surface would be 25 K at that distance (Meech & Svoren 2004).

It is also possible that CO$_2$ sublimation may lift optically detectable grains as far out as 20 au; however, the light curve and active fraction suggest that the sublimation on 2009 MS9, if present, would be dominated by CO. Regardless of the volatile species, the simplest explanation for this delay in the onset of activity is if the volatiles were buried at a depth beneath the surface. Using the delay of the onset of activity, we can solve for the depth using the 1D heat conduction equation subject to a time variable surface boundary temperature condition as the comet moves along its orbit. This method has been used for other comets to estimate the depth of volatiles and has been shown to agree with results obtained by more sophisticated thermal modeling (Meech et al. 2016).

The 1D heat equation is

$$\frac{\partial T}{\partial t} = k \frac{\partial^2 T}{\partial z^2}, \quad (11)$$

where k W cm^{-1} $\times$ K is the thermal conductivity of the comet and is represented by

$$k = \frac{I^2}{\rho C_p}, \quad (12)$$

where ρ is the nucleus density (kg m^{-3}), I is the object's thermal inertia (J K^{-1} m^{-2} s$^{-0.5}$), and c_p is the heat capacity
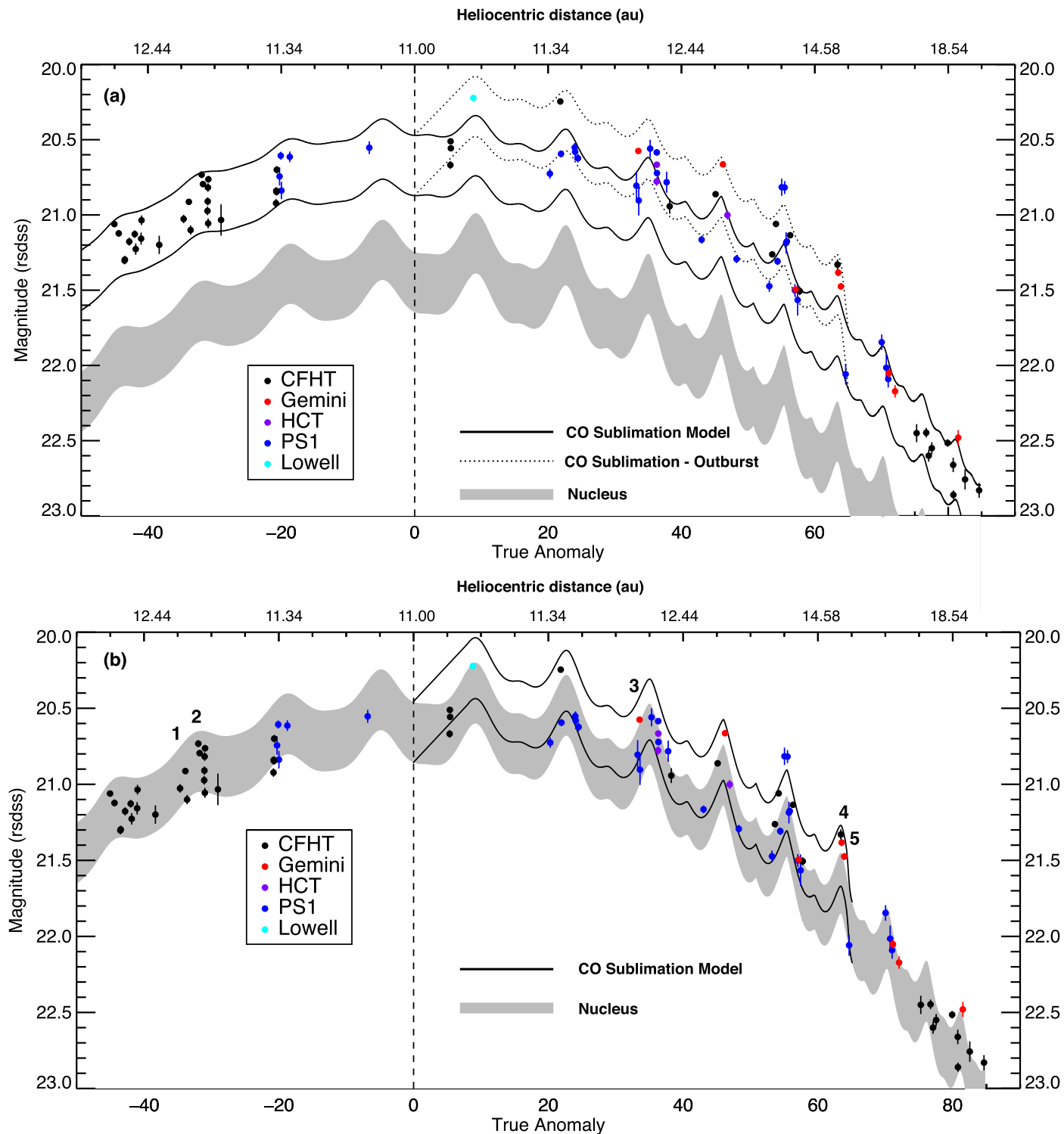
Figure 6. Photometric *r*-band light curve of 2009 MS9 as a function of its orbit assuming CO sublimation for two different activity scenarios. The 0.4 mag variation of 2009 MS9 encloses a range of magnitudes (the gray shaded region represents the nucleus). (a) Modeling CO sublimation pre- and post-perihelion. A baseline FAA of $2.5 \times 10-5$ (black line) is needed, an FAA of $4 \times 10-5$ (dotted line) post-perihelion to match the photometry. An arbitrary nucleus size of 8 km (gray) is shown. (b) CO sublimation (black line) post-perihelion with an FAA of 5×10^{-6} assuming prior inactivity. The nucleus is 11.5 km (gray) from WISE.

($J kg^{-1} K^{-1}$). The latter two have been determined for comet 67P/Churyumov–Gerasimenko by the Rosetta mission, where I has a range of values of $10 J K^{-1} m^{-2} s^{-0.5} < I < 50 J K^{-1} m^{-2} s^{-0.5}$ and $c_p = 500 J kg^{-1} K^{-1}$ (Alí-Lagoa 2015;

Gulkis et al. 2015), which are in agreement with measurements reported from the Deep Impact and Stardust-NExT missions (Groussin et al. 2013). For simplicity, we use a thermal inertia of $I = 10 J K^{-1} m^{-2} s^{-0.5}$ for our modeling.
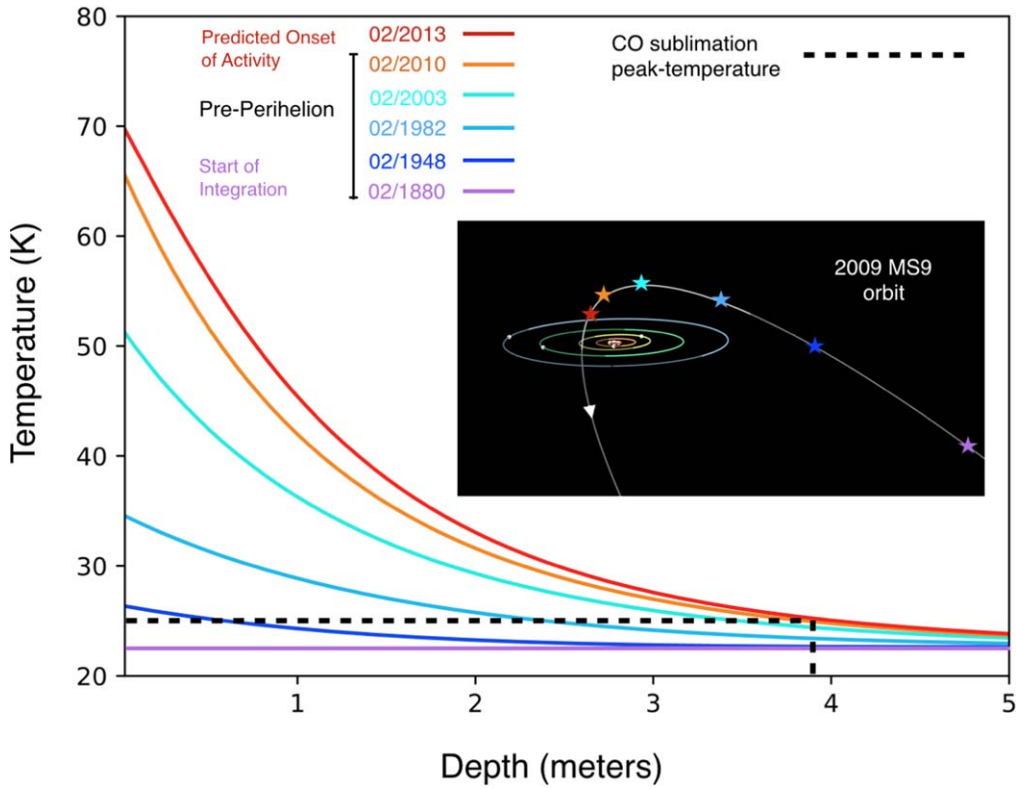
Figure 7. Temperature profile as a function of depth for different positions (color coded in the main panel and matched to the stars of the same color scheme in the inset panel) along the orbit of comet 2009 MS9. As 2009 MS9 gets closer to the Sun, the temperature at its surface increases, and this propagates to the interior following 1D heat conduction. We map the temperature profile of the near surface of the comet by integrating from 1880, where the object is too far (130 au) to start CO sublimation, up until perihelion in 2013 with integration steps of 1 day. At the object's perihelion is where we predict the onset of activity, and at this time, the depth with the temperature corresponding to peak CO sublimation (25 K) is ≈3.9 m from the surface.

To solve the 1D heat conduction equation, we use a Crank–Nicholson scheme, such that

$$-rT_{i+1}^{n+1} + (1 + 2r)T_i^{n+1} - rT_{i-1}^{n+1}$$
$$= rT_{i+1}^n + (1 - 2r)T_i^n + rT_{i-1}^n. \qquad (13)$$

The value r is a unitless numerical constant that is equal to $\frac{\Delta t}{1\rho c_p \Delta x^2}$, i refers to the spatial step starting from the surface to the interior of the comet, and n refers to the time step of the equation. This is a second-order implicit numerical scheme that uses the central difference between spatial steps to numerically solve the equation for the thermal profile at the next time step. It is found to be unconditionally stable for values of r less than 1. We use time steps of 0.25 day, or 6 hr, and spatial steps of 0.001 m down to a depth of 100 m for our calculation.

The outer boundary condition of the temperature at the surface of the comet, T_{eq}, is a function of the comet's heliocentric distance. It is the effective temperature at the surface of the comet at its position along the orbit, and it is represented by

$$T_{eq} = T_\odot (1 - p_v)^{\frac{1}{4}} \sqrt{\frac{R_\odot}{2d}}, \qquad (14)$$

where $T_\odot$ is the temperature at the surface of the Sun, $R_\odot$ is the radius of the Sun, d is the heliocentric distance, and p_v is the albedo of the comet.

We start the numerical integration in 1880 (Figure 7, purple) because at this time, 2009 MS9 was at 130 au, and this is colder than the temperature required for CO sublimation. We integrate

until 2009 MS9 reaches its perihelion (Figure 7, red), which is our predicted epoch for the onset of activity, to determine the depth that reaches the critical temperature for CO sublimation (which is at 25 K; Figure 7, dashed line).

At 2009 MS9's perihelion on 2013 February 13 at 11 au, we find that the depth of the CO ice layer that reaches the limit of 25 K for CO sublimation is just ∼4 m below the surface.

3.7. Spectral Reflectivity

The spectral reflectivity at each wavelength was calculated relative to the SDSS g filter using the following equations:

$$R_\lambda = \frac{10^{-0.4[m_\lambda - m_\lambda(\odot)]}}{10^{-0.4[m_g - m_g(\odot)]}}, \qquad (15)$$

$$\sigma_{R\lambda} = 0.921\,03\,R_\lambda[\sigma_\lambda^2 + \sigma_g^2 + \sigma_\lambda(\odot)^2 + \sigma_g(\odot)^2]^{0.5}. \qquad (16)$$

In these equations, m_λ is the magnitude in the bandpass, σ_λ is the error on m_λ, σ_r is the error on m_r, and $m_\lambda(\odot)$ is the absolute magnitude of the Sun in that bandpass with error $\sigma_\lambda(\odot)$. We use $m_g(\odot) = 5.12 \pm 0.02$, $m_r(\odot) = 4.69 \pm 0.03$, $m_i(\odot) = 4.57 \pm 0.03$, and $m_z(\odot) = 4.60 \pm 0.03$.

The spectral slope, S, between two filters normalized at filter g is calculated with the following relation:

$$S_g = \frac{10^5}{\lambda - \lambda_g}(-1 + 10^{-0.4((m_\lambda - m_g) - (m_\lambda(\odot) - m_g(\odot)))}), \qquad (17)$$

where λ is in units of angstroms, and S is in units of $\%/10^3$ Å. Because there are more than two filters that make up 2009 MS9's spectral reflectivity, we measure the spectral slopes
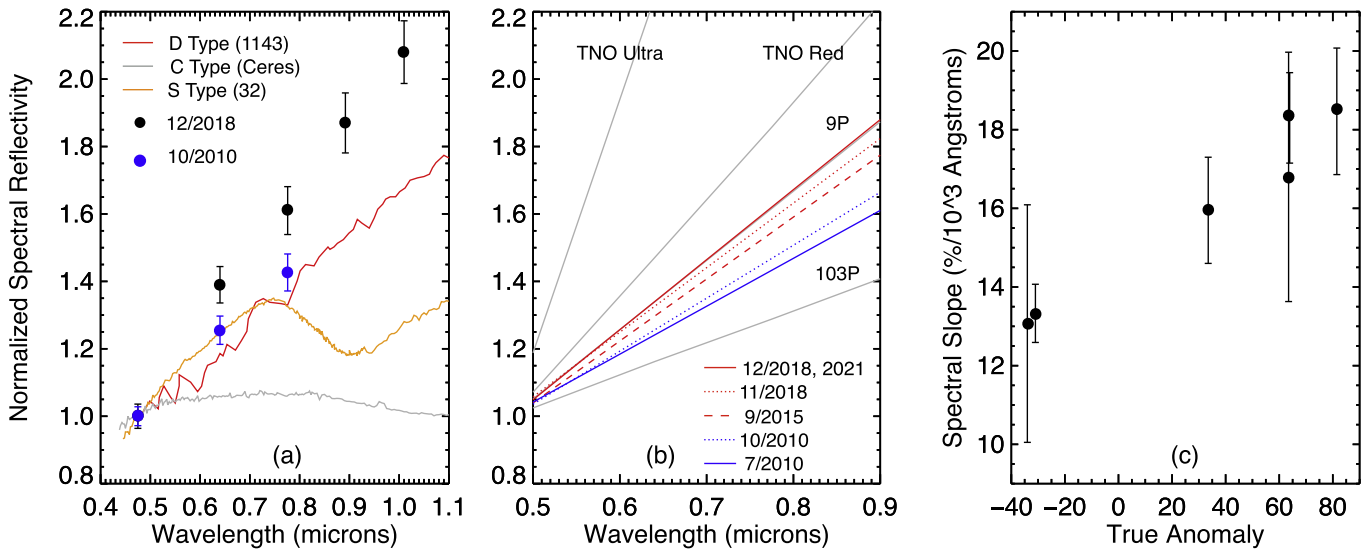
Figure 8. (a) 2009 MS9 colors pre- and post-perihelion in comparison to various SMASS-2 spectral types of other primitive bodies. The spectral reflectivity indicates a surface that is analogous to D-type asteroids. Pre-perihelion 2009 MS9's colors (blue) are bluer in comparison to its colors post-perihelion (black). (Note that the 12/2018 observation refers to the observation taken on 2018 November 30. It is abbreviated to distinguish it from the observation earlier in the month taken 2018 November 10.) (b) 2009 MS9's spectral slope has subtle changes over time that indicate redder colors post-perihelion, when we believe the target to be active. (c) Comparing 2009 MS9's spectral slopes and their error to one another as a function of time suggests that the target is redder when active; however, this result is not statistically significant. The numbers refer to the epoch of 2009 MS9's orbit in which the colors were measured, which is shown in Figure 6.

Table 4
2009 MS9 Colors and Spectral Slopes

Date	Telescope	$g - r$	$r - i$	$i - Z$	$Z - Y$	S_g (%/10³ Å)	S_V (%/10³ Å)
7/2010	CFHT	0.64 ± 0.02	0.37 ± 0.02	⋯	⋯	14.53 ± 3.71	13.07 ± 3.02
10/2010	CFHT	0.66 ± 0.01	0.33 ± 0.01	⋯	⋯	14.82 ± 0.92	13.33 ± 0.74
9/2015	Gemini	0.74 ± 0.02	0.24 ± 0.02	0.27 ± 0.02	⋯	18.13 ± 1.73	15.95 ± 1.35
11/2018	Gemini	0.77 ± 0.03	0.22 ± 0.03	0.34 ± 0.03	-0.33 ± 0.05	19.81 ± 3.59	16.80 ± 3.17
12/2018	Gemini	0.80 ± 0.02	0.27 ± 0.02	0.19 ± 0.02	-0.16 ± 0.04	21.22 ± 1.56	18.30 ± 1.15
12/2021	Gemini	0.798 ± 0.03	0.291 ± 0.04	0.13 ± 0.04	⋯	21.46 ± 2.17	18.47 ± 1.61

Note. The table is split into observations pre- and post-perihelion, indicated by double horizontal lines. The 12/2018 observation refers to the 2018 November 30 observation. It is abbreviated to distinguish it from the observation earlier in the month taken on 2018 November 10.

normalized to the g filter for all of the corresponding filters (e.g., r, i, z, and Y, if applicable) and then calculate the average spectral slope for each observation date. We compared this method to the traditional method of calculating the spectral slope by fitting a least-squares line to the normalized reflectivity. The two techniques yield comparable values to within $1\%/10^3$ Å.

To compare our spectral gradients to TNOs and comets in the literature, we change our normalized filter to V using the following equation:

$$S_V = \frac{S_g}{1 + \frac{\lambda_V - \lambda_g}{10^5} S_g}. \qquad (18)$$

We collected six sets of colors for 2009 MS9 using either Gemini or CFHT at different epochs of the target's orbit that are displayed in Table 4. Two are pre-perihelion, and four are post-perihelion. On nights where multiple color sets (i.e., gri color sequences) were taken (e.g., 2010 July 15 and 2010 October 1–6), we take the average color per night minus the magnitude variation due to the 0.4 mag rotation

(Petit et al. 2017). For post-perihelion observations with Gemini, we correct the magnitudes for the 0.4 mag rotation by interweaving the g filter between the other filters, fitting a linear model to the change in g magnitudes over time and subtracting this from the measured magnitudes. The change in g for each Gemini observation is consistent with the 0.4 mag difference observed by Petit et al. (2017).

We compare 2009 MS9's spectral reflectivity to a few SMASS-2 asteroid surfaces (Bus & Binzel 2002) and find that, like comets and other outer solar system bodies, its surface is similar to D-type asteroids in that the slope of the data points is red and lacking a 1 μm absorption dip. However, it appears to have a spectral slope that changes over time. Figure 8(a) shows the maximum difference in spectral slope between 2009 MS9 pre- and post-perihelion in comparison to asteroid types.

The orbital properties of 2009 MS9 put it in a unique position to straddle the boundary between different dynamical classes of minor bodies, specifically LPCs and TNOs (Figure 8(b)). Because of this, we compare 2009 MS9's changing colors to both types of objects. Pre-perihelion 2009 MS9 is closer to the colors of short-period comet (SPC) 103P-

Hartley (Li et al. 2013). Post-perihelion, the colors appear redder, as the spectral slope increases to resemble that of SPC 9P (Li et al. 2007). The complete evolution of the six reflectivities is shown in Figure 8(b) in comparison to TNO and comet colors. In comparison to red and ultrared TNOs, 2009 MS9 is considered "gray" (Delsanti et al. 2004; see Section 4.1 for further discussion). The corresponding spectral slope as a function of orbit is shown in Figure 8(c). There appears to be a linear increase in spectral slope as 2009 MS9 moved throughout its orbit.

4. Discussion

4.1. Colors in Comparison to TNOs

The TNOs include minor solar system bodies orbiting the Sun with a semimajor axis greater than that of Neptune, most of which belong to the Kuiper Belt. The Kuiper Belt has been found to have two major dynamical classes: the classical "cold" objects distributed near inclinations of 3° and the dynamically excited "hot" objects or scattered objects with a broad range of inclinations (Brown 2001). These two populations are also distinguished by their colors. Studies have consistently shown that dynamically excited TNOs are less red than the cold classical population, and that color is specifically correlated with inclination (Tegler & Romanishin 1998, 2000; Tegler et al. 2005; Hainaut et al. 2012; Marsset et al. 2019).

The dichotomy of colors and orbital types for TNOs is seen as a precursor for the dichotomy of colors of Centaurs, which are minor bodies that are thought to be the next evolutionary step after a TNO is perturbed out of the Kuiper Belt and sent on a shorter-period, less stable planet-crossing orbit (Tegler et al. 2016). However, one very important question remains: is this observed color and orbital dichotomy for TNOs and Centaurs indicative of evolutionary change, or does it represent a difference in origin and/or composition for these minor bodies?

Historically, Jewitt & Luu (2001) predicted that irradiation and cratering of the surface was responsible for the large distribution of TNO colors. However, this was shown to be implausible by Tegler et al. (2003), who were the first to statistically prove that the TNO population exhibited a color bimodality and that its homogeneous surface colors pointed to gray impact craters on radiation-reddened crusts being an unlikely physical driver for color differences.

Wong & Brown (2017) theorized that the cause of the bimodal of color distribution observed in the Kuiper Belt stems from the retention of volatiles in some Kuiper Belt objects (KBOs), whereas others do not retain their volatiles because they migrated in the protoplanetary disk during the solar system's formation. They stipulated that KBOs that acquired volatiles at the surface became irradiated and thus redder, which could explain the split between gray and red surfaces.

Our work shows that 2009 MS9, an extreme TNO closest in orbital properties to the hot dynamically excited KBOs, has an albedo of 0.25 that is comparable to the range of albedos observed for other TNOs (Jewitt 2015) and a "gray" surface that becomes red after sublimation. The change in spectral slope for 2009 MS9 (from 13% to 18%/10^3 Å; Figure 8, Table 4) brings it closer to the observed split between "gray" dynamically excited KBOs and "red" cold classical KBOs at 20%/10^3 Å , observed by Marsset et al. (2019).

The LPCs often change their orbital properties after sufficient close planetary passes. The same may be true for 2009 MS9, whose perihelion falls close to the outer three gas giants. To investigate this further, future work must be done to simulate 2009 MS9's orbit to see if such passages exist. If they do, this plus the evidence for sublimation may eventually place it in the regime of "red" cold classical KBOs. Like Wong & Brown (2017), we theorize that volatiles play a role in creating the two color populations observed in the Kuiper Belt. However, we suggest that sublimation and orbital evolution are the driving factors for the two color classes of KBOs.

4.2. Evidence for Activity-driven Surface Evolution

While it has been predicted that the color differences in the TNO population arise from the retention of volatiles from different formation environments (Wong & Brown 2017), we suspect that the color changes (reddening) of TNOs may be sublimation-driven based on the activity of our target. Specifically, the reddening of 2009 MS9 arises from the buildup of a dust mantle at the surface of the comet.

The colors of 2009 MS9 are very similar to the spectral reflectivity of known Jupiter-family comets (Li et al. 2013; Kelley et al. 2017). However, 2009 Ms9's reddening post–sublimation onset is contrary to what is seen for other comets when they become active. For example, the surface colors of 67P and C/2017 K2 became bluer as the comets approach perihelion and activity deposits fresh ice on the surface; this was observed in situ for comet 67P (Fornasier et al. 2016; Meech et al. 2017). One explanation for 2009 MS9's reddening when it appears to be active is the buildup of large grains brought to the surface from interior sublimation. When subsurface sublimation occurs, it has the potential to bring a variety of grains, including large (millimeter+) dust grains, through the porous interior to the surface, where they may not be ejected into a dust tail because there is not enough force to lift them from the surface or the gas drag cannot accelerate them to a velocity higher than the escape velocity (and they fall back onto the surface; Prialnik et al. 2004). This process can create a dust mantle or crust that is redder than the prior surface due to the deposition of organic-rich large grains that cover (or deplete) the ice at the surface (Prialnik et al. 2004). Additionally, large grains also have the potential to clog the comet porous medium, which may quench activity (Prialnik et al. 2004). This may explain why 2009 MS9 had a delay in the onset of activity and why it is no longer active now.

To investigate the concept of a dust mantle further, we have to consider the behavior of all grain sizes for 2009 MS9. Our sublimation and dust models assume one grain size for activity; however, previous studies of active bodies, including space-craft missions, suggest that there is a range of submicron- to centimeter-sized grains making up the nuclei (surface + subsurface) of small bodies that contribute to the dust tail during periods of activity (Meech & Svoren 2004; Prialnik et al. 2004). Due to the effects of scattering, grain sizes on the order of an observation's wavelength are most likely to be detected. Thus, in the optical, micron-sized grains should dominate in the observed dust tails of active bodies. The grain size distribution in the dust tail follows a power law such that $f(r) \propto r^n$, where r is the radius of the grain. The power-law index observed for previous SPCs is, on average, $n = -3.5$ (Fulle 2004). If $n > -3.5$, then this implies that the brightness

of the target from the dust tail is dominated by the scattering of the largest grains, even if observed in the optical (Fulle 2004).

The power index (whether measured as an average or time-dependent) is difficult to measure robustly for LPCs and other active bodies in the absence of in situ spacecraft missions. We might expect that the difference in formation environment and dynamical evolution between LPCs and SPCs may in turn cause different average indexes and size limits for each of these populations. For example, in Tony Farnham's thesis (1998), using a dust model that is described in Chu et al. (2020), he shows that dynamically new LPC comet Torres has a dust distribution that follows a power law with $n = 1.1$ and, further, is unexpectedly devoid of micron-sized particles.

During the formation of a dust mantle, small grains (i.e., micron-sized) will move more easily through the porous medium of the interior and are more likely to be ejected from the surface. This is because their velocity will be closer to the gas drag due to their higher acceleration in comparison to large grains.

So the question is: where are these micron-sized grains for 2009 MS9? There are two hypotheses for this.

1. There are not enough small grains to be detected in deep images.
2. The small grains simply are not there.

Both theories can be investigated with an order-of-magnitude approximation of what average dust production rate we would expect based on the window of observation for activity and the power law for the distribution of grain sizes. To a first approximation, to form a dust mantle, the entire surface of the comet is covered in large grains that are small enough to travel through the porous interior, for example, millimeter-sized. If we assume that the shape of 2009 MS9 and the dust grains is spherical, then we would need grains of 10^{14} mm in size to cover the surface.

Assuming a power law of $n = -3.5$ for typical SPCs, this means that 10^{23} μm–sized grains would be present and ejected from the surface. Next, assume that each grain has a density of $2.2\,\mathrm{g\,m^{-3}}$ based on the average density of common materials on small bodies (Mukai 1989; Grün & Jessberger 1990) and multiply this by the volume of one micron-sized spherical grain and the number of micron-sized grains to get the total mass of small grains. If we assume that grains were emitted from the nucleus as early as 2009, our observation window to detect activity is 13 yr. Dividing our total mass by this gives us an average dust production rate of $\approx 10\,\mathrm{kg\,s^{-1}}$. This is higher than the limit we place on dust production using our surface brightness profiles and what our sublimation model predicts. If a power-law index of $n = -3.5$ is true, this suggests we should be detecting micron-sized dust. Since we are not, the micron-sized dust grains must not be there; perhaps they were ejected and dispersed before the first observation 13 yr ago.

If we consider a higher index value for our power law, namely, $n = -2.5$, this yields an average dust production of $0.06\,\mathrm{kg\,s^{-1}}$ for micron-sized grains. Note that this is consistent with what the sublimation model predicts and is less than the limits that we have placed on the dust production rate for micron-sized grains using our surface brightness profiles. This would suggest that the small dust is present but does not have a high enough dust production rate to produce an observable dust tail in the images.

Adopting a power-law index of -2.5 is compatible with theory 1, while a traditional index of -3.5 suggests that theory 2 is more likely. Unfortunately, in order to ascertain a precise and accurate value of the power-law index, we need to detect and model the dust, which is something we are not able to do at this time (but may be able to do with future JWST observations). Nonetheless, the observation of our target's color changes (reddening) and the outburst of sublimation post-perihelion suggesting volatiles at a depth combined with either the absence of small grains or a power law > -3.5 suggests that the buildup of a dust mantle as a result of cometary surface/subsurface evolution is highly likely. We would expect the volatiles to retreat further into the nucleus for future orbital iterations as the dust mantle builds up and the layer of ice depletes (Prialnik et al. 2004).

5. Summary

Recently, astronomers have tried to directly detect activity in the Kuiper Belt, as it is another abundant reservoir for icy bodies; however, most KBOs are too faint for a coma to be observed. With newer, deeper surveys like PS1 and ATLAS, we are able to study and discover these faint objects more efficiently, allowing us to examine volatiles over a larger range of distances. One of these objects of interest is 2009 MS9, as it is classified as a TNO with a comet-like orbit that places its perihelion at 11 au, where comets have been observed to become active. At these distances, we can observe CO and CO_2 ice sublimation without the contamination of water ice, which activates at closer distances to the Sun. This allows us to characterize the activity of 2009 MS9 and other TNOs that have sublimation associated with more volatile species, which is important in understanding the distribution and roles of volatile transport during solar system formation and evolution.

Our light curve constructed from a suite of professional telescopes is not compatible with an inert nucleus. We explore this further with composite images + radial flux profiles and sublimation/thermal modeling. With this, we set strong limits on the nucleus radius (>11.5 km) and geometric albedo (0.25), as well as cometary activity (dust + outgassing). The nondetection of dust in composite images suggests that large grains dominate the activity. We confirm that 2009 MS9 must be active with a hypervolatile species (CO or CO_2) and that this ice exists at a depth. The behavior of the light curve suggests CO as the dominant volatile species. If active with CO, this activity is quenched near 15 au post-perihelion.

Like other comets, 2009 MS9 exhibits colors analogous to D-type asteroids. When compared to other KBO colors, 2009 MS9 is considered "gray." However, the surface colors of our target changed throughout its orbit. Pre- versus post-perihelion color evolution brings it closer to the observed boundary between "gray" and "red" KBOs. This suggests that sublimation may play an important role in creating the dichotomy of colors observed in the Kuiper Belt. Lastly, the timing of the color change combined with the proposed activity and presence of large grains suggests the accumulation of a dust mantle on the surface of 2009 MS9.

When JWST launches, we will have the opportunity to constrain the colors of the target through spectra. Object 2009 MS9 will remain observable by large telescopes such as Gemini and CFHT until it reaches 24th magnitude in 2027; however, it may be observable by LSST and JWST until the

object reaches 27th magnitude in 2040, which is the limiting magnitude of the stacked images of LSST.

ORCID iDs

Erica Bufanda https://orcid.org/0000-0002-0406-8518
Karen J. Meech https://orcid.org/0000-0002-2058-5670
Jan T. Kleyna https://orcid.org/0000-0002-4734-8878
Olivier R. Hainaut https://orcid.org/0000-0001-6952-9349
James M. Bauer https://orcid.org/0000-0001-9542-0953
Haynes Stephens https://orcid.org/0000-0003-0425-5265
Marco Micheli https://orcid.org/0000-0001-7895-8209
Jacqueline V. Keane https://orcid.org/0000-0002-2021-1863
Robert Weryk https://orcid.org/0000-0002-0439-9341
Richard Wainscoat https://orcid.org/0000-0002-1341-0952
Devendra K. Sahu https://orcid.org/0000-0002-6688-0800
Bhuwan C. Bhatt https://orcid.org/0000-0003-0174-3829

References

A'Hearn, M. F., Millis, R. C., Schleicher, D. O., Osip, D. J., & Birch, P. V. 1995, Icar, 118, 223
Alí-Lagoa, V., Delbo', M., & Libourel, G. 2015, ApJL, 810, L22
Bar-Nun, A., Dror, J., Kochavi, E., & Laufer, D. 1987, PhRvB, 35, 2427
Bauer, J. M., Stevenson, R., Kramer, E., et al. 2015, ApJ, 814, 85
Bertin, E. 2010, SWarp: Resampling and Co-adding FITS Images Together, ascl:1010.068
Bertin, E., & Arnouts, S. 1996, A&AS, 117, 393
Brown, M. E. 2001, AJ, 121, 2804
Bus, S. J., & Binzel, R. P. 2002, Icar, 158, 146
Chambers, K. C., Magnier, E. A., Metcalfe, N., et al. 2016, arXiv:1612.05560
Chu, L. E. U., Meech, K. J., Farnham, T. L., et al. 2020, Icar, 338, 113532
Delsanti, A., Hainaut, O., Jourdeuil, E., et al. 2004, A&A, 417, 1145
Denneau, L., Jedicke, R., Grav, T., et al. 2013, PASP, 125, 357
Fernández, Y. R., Kelley, M. S., Lamy, P. L., et al. 2013, Icar, 226, 1138
Finson, M. J., & Probstein, R. F. 1968, ApJ, 154, 327
Flewelling, H. A., Magnier, E. A., Chambers, K. C., et al. 2020, ApJS, 251, 7
Fornasier, S., Mottola, S., Keller, H. U., et al. 2016, Sci, 354, 1566
Fulle, M. 2004, in Comets II, ed. M. C. Festou, H. U. Keller, & H. A. Weaver (Tucson, AZ: Univ. Arizona Press), 565
Fulle, M., Marzari, F., Della Corte, V., et al. 2016, ApJ, 821, 19
Gladstone, G. R., & Young, L. A. 2019, AREPS, 47, 119
Groussin, O., Lamy, P., Jorda, L., & Toth, I. 2004, A&A, 419, 375
Groussin, O., Sunshine, J. M., Feaga, L. M., et al. 2013, Icar, 222, 580
Grün, E., & Jessberger, E. K. 1990, in Physics and Chemistry of Comets, Astronomy and Astrophysics Library, ed. W. F. Huebner (Berlin: Springer), 113
Gulkis, S., Allen, M., von Allmen, P., et al. 2015, Sci, 347, aaa0709
Hainaut, O. R., Boehnhardt, H., & Protopapa, S. 2012, A&A, 546, A115
Hainaut, O. R., Delahodde, C. E., Boehnhardt, H., et al. 2000, A&A, 356, 1076
Harris, A. W. 1998, Icar, 131, 291
Hook, I. M., Jørgensen, I., Allington-Smith, J. R., et al. 2004, PASP, 116, 425
Jewitt, D. 2015, AJ, 150, 201
Jewitt, D. C., & Luu, J. X. 2001, AJ, 122, 2099
Jones, R. L., Gladman, B., Petit, J. M., et al. 2006, Icar, 185, 508
Jorda, L., Gaskell, R., Capanna, C., et al. 2016, Icar, 277, 257
Kelley, M. S., Woodward, C. E., Gehrz, R. D., Reach, W. T., & Harker, D. E. 2017, Icar, 284, 344
Krasnopol'Skii, V. A., Moroz, V. I., Krysko, A. A., Tkachuk, A. Y., & Moreels, G. 1987, A&A, 187, 707
Labrie, K., Anderson, K., Cárdenes, R., Simpson, C., & Turner, J. E. H. 2019, in ASP Conf. Ser. 523, Astronomical Data Analysis Software and Systems XXVII, ed. P. J. Teuben et al. (San Francisco, CA: ASP), 321
Lebofsky, L. A., Sykes, M. V., Tedesco, E. F., et al. 1986, Icar, 68, 239
Li, J.-Y., A'Hearn, M. F., Belton, M. J. S., et al. 2007, Icar, 191, 161
Li, J.-Y., Besse, S., A'Hearn, M. F., et al. 2013, Icar, 222, 559
Lisse, C. M., Fernandez, Y. R., Reach, W. T., et al. 2009, PASP, 121, 968
Lupton, R. 2005, Transformations between SDSS magnitudes and UBVR_cI_c, http:3//classic.sdss.org/dr4/algorithms/sdssUBVRITransform.html#Lupton2005
Magnier, E. A., Schlafly, E. F., Finkbeiner, D. P., et al. 2020, ApJS, 251, 6
Mainzer, A., Bauer, J., Cutri, R. M., et al. 2014, ApJ, 792, 30
Mainzer, A., Grav, T., Bauer, J., et al. 2011, ApJ, 743, 156
Marsset, M., Fraser, W. C., Pike, R. E., et al. 2019, AJ, 157, 94
Meech, K. J., Hainaut, O. R., Boehnhardt, H., & Delsanti, A. 2003, EM&P, 92, 169
Meech, K. J., & Jewitt, D. C. 1987, A&A, 187, 585
Meech, K. J., Jewitt, D., & Ricker, G. R. 1986, Icar, 66, 561
Meech, K. J., Pittichová, J., Bar-Nun, A., et al. 2009, Icar, 201, 719
Meech, K. J., Schambeau, C. A., Sorli, K., et al. 2017, AJ, 153, 206
Meech, K. J., & Svoren, J. 2004, in Comets II, ed. M. C. Festou, H. U. Keller, & H. A. Weaver (Tucson, AZ: Univ. Arizona Press), 317
Meech, K. J., Yang, B., Kleyna, J., et al. 2016, SciA, 2, e1600038
Mekler, Y., & Podolak, M. 1994, P&SS, 42, 865
Mukai, T. 1989, in Evolution of Interstellar Dust and Related Topics, ed. A. Bonetti, J. M. Greenberg, & S. Aiello (Amsterdam: Elsevier), 397
Petit, J. M., Kavelaars, J. J., Gladman, B. J., et al. 2017, AJ, 153, 236
Piro, C., Meech, K. J., Bufanda, E., et al. 2021, PSJ, 2, 33
Prialnik, D., Benkhoff, J., & Podolak, M. 2004, in Comets II, ed. M. C. Festou, H. U. Keller, & H. A. Weaver (Tucson, AZ: Univ. Arizona Press), 359
Reach, W. T., Kelley, M. S., & Vaubaillon, J. 2013, Icar, 226, 777
Schlafly, E. F., Finkbeiner, D. P., Jurić, M., et al. 2012, ApJ, 756, 158
Sekiguchi, T., Boehnhardt, H., Hainaut, O. R., & Delahodde, C. E. 2002, A&A, 385, 281

Shappee, B., Prieto, J., Stanek, K. Z., et al. 2014, AAS Meeting Abstracts, 223, 236.03

Slemp, L. A., Meech, K. J., Bufanda, E., et al. 2022, PSJ, 3, 34

Snodgrass, C., Tubiana, C., Bramich, D. M., et al. 2013, A&A, 557, A33

Stansberry, J., Grundy, W., Brown, M., et al. 2008, in The Solar System Beyond Neptune, ed. M. A. Barucci et al. (Tucson, AZ: Univ. Arizona Press), 161

Tegler, S. C., & Romanishin, W. 1998, Natur, 392, 49

Tegler, S. C., & Romanishin, W. 2000, Natur, 407, 979

Tegler, S. C., Romanishin, W., & Consolmagno, G. J. 2003, ApJL, 599, L49

Tegler, S. C., Romanishin, W., Consolmagno, G. J., & J. S., 2016, AJ, 152, 210

Tegler, S. C., Romanishin, W., Consolmagno, G. J., et al. 2005, Icar, 175, 390

Thomas, P., A'Hearn, M., Belton, M. J. S., et al. 2013a, Icar, 222, 453

Thomas, P. C., A'Hearn, M. F., Veverka, J., et al. 2013b, Icar, 222, 550

Tonry, J. L., Stubbs, C. W., Lykke, K. R., et al. 2012, ApJ, 750, 99

Tonry, J. L., Denneau, L., Heinze, A. N., et al. 2018, PASP, 130, 064505

Weryk, R. J., Lilly, E., Chastel, S., et al. 2016, arXiv:1607.04895

Wong, I., & Brown, M. E. 2017, AJ, 153, 145

Wright, E. L. 2007, arXiv:astro-ph/0703085

Wright, E. L., Eisenhardt, P. R. M., Mainzer, A. K., et al. 2010, AJ, 140, 1868

Yang, B., Keane, J., Meech, K., Owen, T., & Wainscoat, R. 2014, ApJL, 784, L23

Young, L. A., Braga-Ribas, F., & Johnson, R. E. 2020, in The Trans-Neptunian Solar System, ed. D. Prialnik, M. A. Barucci, & L. Young (Amsterdam: Elsevier), 127